Perforation of 6082-T651 Aluminum Plates with 7.62mm APM2 Bullets at Normal and Oblique Impacts

M.J. Forrestal • T. Børvik • T.L. Warren • W. Chen

Abstract We conducted an experimental study to understand the mechanisms and dominant parameters for 7.62mm APM2 bullets that perforate 6082-T651 aluminum armor plates at oblique impacts. The 7.62-mm-diameter, 10.7g, APM2 bullet consists of a brass jacket, lead filler, and a 5.25g, ogive-nose, hard steel core. The brass and lead were stripped from the APM2 bullets by the targets, so we conducted ballistic experiments with both the APM2 bullets and only the hard steel cores. These projectiles were fired from a rifle to striking velocities between 400 and 1,000m/s into 20-mm-thick plates at normal impact ($\beta=0^{o}$) and at oblique angles of $\beta=15^{o}$, 30°, and 45°. Measured residual and ballistic-limit velocities for the full bullet and the hard core were within a few percent for normal impact and all oblique angles. Thus, we showed that the perforation process was dominated by the hard steel core of the bullet. In addition, we conducted large strain, compression tests on the 6082-T651 plate material for input to perforation equations derived from a cavity-expansion model for the steel core projectiles. Model predictions were shown to be in good agreement with measured ballistic-limit and residual velocity measurements for $\beta=0^{o}$, 15°, and 30°. We also presented a scaling law for the bullet that showed the ballistic-limit velocities were proportional to the square root of the product of plate thickness and a material strength term.

Keywords 7.62mm APM2 bullets • Aluminum armor plates • Oblique impacts • Experimental study • Perforation equations

_____

M. J. Forrestal (SEM member)

3029 Tanglewood Park W., Fort Worth, TX 76109, USA.

e-mail: mjforrestal@gmail.com

T. Børvik

Structural Impact Laboratory (SIMLab), Centre for Research-based Innovation (CRI), Department of

Structural Engineering, Norwegian University of Science and Technology, NO-7491 Trondheim, Norway and

Norwegian Defence Estates Agency, Research and Development Department, NO-0015 Oslo, Norway.

e-mail: tore.borvik@ntnu.no

T.L. Warren (SEM member and corresponding author)

3804 Shenandoah Pl, NE, Albuquerque, NM 87111, USA.

e-mail: tlwarre@msn.com

W. Chen (SEM member)

Schools of Aeronautics/Astronautics and Materials Engineering

Purdue University, West Lafayette, IN 47907, USA.

e-mail: wchen@purdue.edu

Introduction

Several authors have published recent studies on the perforation of aluminum plates with 7.62mm APM2 bullets at normal impact. All these studies present experimental data, and some studies include numerical simulations or analytical models. Gooch et al. [1,2] report ballistic-limit data for 6061-T651 and 5083-H131 target plates with thicknesses between 25-57mm. Borvik et al. [3] performed tests at a striking velocity of 830m/s into 20-mm-thick, 6082-T4 plates and conducted finite-element simulations. Holmen et al. [4] present residual velocity versus striking velocity data and finite-element simulations for 20-mm-thick, AA6070 plates with four different heat treatments.

We conducted our previous experimental and analytical studies to better understand the perforation process and identify the dominant problem parameters for normal impact. Experiments were conducted at normal impacts into 5083-H116 [5] and 7075-T651 [6] targets with the 7.62mm APM2 bullet and only the hard steel core contained in the bullet. Data from both sets of experiments showed only small differences in residual and ballistic-limit velocities for the full bullet and the hard steel core projectiles. Thus, the hard steel core dominated the perforation process. In addition, we performed large strain, compression tests on the aluminum target materials for input to perforation equations derived from a cylindrical cavity-expansion analysis. Model predictions were in good agreement with measured residual and ballistic-limit velocities for the hard steel core projectiles. References [1-6] focus on the normal impact problem.

For this paper, we conducted ballistic tests into 20-mm-thick , 6082-T651 aluminum plates with 7.62mm APM2 bullets and the hard steel cores for normal impact ($\beta=0^o$) and at oblique angles of $\beta=15^o$, 30°, and 45°. Plots of residual velocity versus striking velocity showed that the data for both the full bullet and hard core projectiles agreed with each other to within a few

percent. We also showed that predictions from our cavity-expansion model for the hard core projectiles were in good agreement with data for $\beta=0^{\circ}$, 15°, and 30°. Unfortunately, there is a misprint in one of the model equations in [5], so we correct that misprint in this paper. In addition, we presented a scaling law that showed the ballistic-limit velocities for five aluminum alloys were proportional to the square root of the product of plate thickness and a target material strength term. The strength term was derived from a cylindrical cavity-expansion analysis that requires large strain compression data.

Projectiles

Figure 1 shows the dimensions and the parts that make up the APM2 bullet. The 7.62mm-diameter, 10.7g, APM2 bullet consists of a brass jacket, an end cap, lead filler, and a 5.25g, ogive-nose, hard steel core. The steel core has a density $\rho_p=7{,}850\text{kg/m}^3$, hardness R_c 63, and $\psi=$CRH $= 3.0$ (caliber-radius-head). The APM2 bullets are carefully produced to tight tolerances so that the bullets properly fit into the bore of the gun barrel. In addition, we show later that these bullet parameters have a square root dependence in the model, so these are not sensitive parameters.

As previously mentioned, we will present predictions from a cylindrical cavity-expansion model for the hard steel core projectile. Our perforation model is for a rigid, ogive-nose, rod projectile. Note that the shank of the steel core of the 7.62mm APM2 bullet shown in Fig. 1 is truncated towards the end cap, so we use an equivalent shank length L that matches the measured mass of the steel core. Properties for the equivalent hard steel core projectile include: mass $m=5.25\text{kg}$, diameter $2a=6.17\text{mm}$, CRH=3.0, nose length $l=10.2\text{mm}$, and shank length $L=16.8\text{mm}$.

AA6082-T651 Target Plates

The 20-mm-thick target plates were obtained from Alcoa Europe. The supplier provided an inspection certificate with tensile test data from four tests in the rolling direction ($\theta=0^o$). The average values for the ultimate tensile strength and yield strength at the 0.2 percent offset were σ_u=300MPa and σ_o=259MPa. In addition, we conducted three tensile tests in the rolling direction ($\theta=0^o$) and also for $\theta=45^o$ and 90°. The average values for $\theta=0^o$, 45°, and 90° were σ_u=290, 290, 297MPa and σ_o=265, 255, 265MPa, respectively. All values of σ_u and σ_o are in close agreement with each other.

We conducted three standard compression tests in each of four directions: the thickness direction, the rolling direction ($\theta=0^o$), and the $\theta=45^o$ and 90° directions. The cylindrical test samples had an initial diameter D_o=10mm and an initial length of L_o=10mm. After grinding the end surfaces, the specimens were precisely aligned between two hard, polished anvils in a servo-hydraulic test machine to obtain a homogenous deformation of the specimen. To minimize the effect of barreling caused by friction between the specimen surfaces and the anvils, a graphite paste was used to lubricate the interfaces. The tests were conducted at room temperature with a constant strain rate of about $10^{-3}s^{-1}$. The force was measured by a calibrated load cell, and the displacement was measured by the actuator stroke and an extensometer attached to the anvils. Based on these measurements, stresses and strains were calculated. Average values for the yield strength at the 0.2 percent offset were σ_o =271, 257, 266, 275MPa for the thickness direction, the rolling direction ($\theta=0^o$), and for $\theta=45^o$ and 90°, respectively. All values of σ_o for the compression tests are in close agreement with each other and the tension data. In addition, we show later that material strength has a square root dependence on the model, so σ_o is not a sensitive parameter.

Kawahara [7] and Lovato and Stout [8] present experimental methods that determine large-strain, uniaxial compression data for metal samples. These authors report true stress versus true strain data to true strains of 1.0. To closely approximate a cylindrical sample that is compressed homogeneously so that all material points have an identical deformation, concentric grooves were machined into the top and bottom of the samples. Then lubrication was placed in the grooves, and the grooves contain the lubrication during sample compression. These techniques provide nearly frictionless surfaces at the sample-platen interfaces and prevent barreling. True stress versus true strain data show that lubricated samples without grooves show negligible barreling to true strains of about 0.2, but the grooved samples are required for true strains from 0.2 to 1.0. In [7,8], the displacement between the platens was measured by an extensometer and strains were calculated from the displacement measurements. The sample is not homogeneous near the grooves, and this could cause errors in strain calculations. In this study, we put grid lines on the sample away from the groves and photographed deformation between the grid lines.

We conducted three tests in the thickness direction and also for the rolling direction ($\theta=0^{\circ}$) and $\theta=90^{\circ}$. Samples had an initial length L_{o}=7.62mm and initial diameter D_{o}=7.62mm. As shown in Fig. 2, the distance between the grid lines was 3.8mm. Three concentric grooves were machined into the top and bottom of the samples to retain lubrication during the compression tests. These grooves were semi-circular in shape with radius 0.254mm. The lubrication was molybdenum disulfide. Grid lines were photographed during compression at a strain rate of about $10^{-3}s^{-1}$. The samples were precisely aligned between two polished anvils in a servo-hydraulic test machine, and force was measured with a calibrated load cell. Stresses and strains were calculated from the force and photographed deformation measurements. Figure 2 shows four of fifteen images taken to a true strain of 0.8. The deformed samples show a nearly homogeneous deformation.

For input to our cavity-expansion perforation model, the uniaxial compression data were curve-fit with

$$\sigma = \begin{cases} E\varepsilon & , \quad \sigma < Y \\ Y\left(\dfrac{E\varepsilon}{Y}\right)^n & , \quad \sigma \geq Y \end{cases} ,$$

(1a,b)

where σ is the true stress, ε is true strain, E is Young's modulus, Y is the yield stress, and n is the strain-hardening exponent. Figure 3 shows this power-law fit and stress-strain data from the rolling direction of the plate with $Y=\sigma_o=265$MPa and a coefficient of determination of 0.9980. Other material properties are given in Fig. 3. As previously mentioned, we conducted three tests in the thickness direction, the rolling direction ($\theta=0^o$) and in the $\theta=90^o$ direction. Results from all nine tests were within a few percent of each other.

The material description for our perforation model is independent of strain rate. As discussed in [4], many experimental studies show that these aluminum alloys are rate insensitive to strain rates of $10^3 s^{-1}$. In addition, we show later that our perforation model is dominated by a quasi-static term, so we neglect strain rate effects in this study and also in our previous papers [5,6].

The 7.62mm APM2 Bullet and Hard Steel Core Experiments

A 7.62-mm-diameter, 63-mm-long, smooth-bore Mauser gun that used adjusted ammunition fired these projectiles. The APM2 bullets fit the gun bore, and the 6.17-mm-diameter cores were encased in a 7.62-mm-diameter, 0.3g plastic sabot. Square target plate configurations with a side length of 300mm and thickness of 20mm were firmly clamped to a frame by two beams. This provided a fixed boundary for the horizontal sides of the targets, while the vertical sides remained free. The in-plane distance between each impact point and the target boundary was 100mm, and a maximum of four shots were allowed in each target before it was replaced.

Striking and residual velocities were measured with laser optical devices that were shown to be accurate to within 1% and 2%. In addition, the overall perforation process was photographed with a high-speed video camera operating at 50,000-100,000 frames per second. Both the experimental procedures and measurements used in these tests are described in more detail in [3,4].

We conducted a large number of ballistic tests with striking velocities V_s between 400-1000m/s. Tables 1 and 2 list the measured striking velocities V_s and residual velocities V_r for normal impacts (β=0°) and oblique impacts with β=15°, 30°, and 45°. Figure 4 shows high-speed video images of the perforation process for a 20-mm-thick plate impacted by the APM2 bullet. Note that the brass jacket and lead cap are completely stripped from the hard core by the target. Figure 5 shows high-speed video images for a 20-mm-thick plate impacted by the hard steel core.

The most important results of our study are shown in Figs. 6-9 that display the residual velocity versus striking velocity curves for β=0°, 15°, 30°, and 45°. Data for the APM2 bullets and hard cores were curve-fit with the least squares method and the Lambert-Jonas empirical equation [9,10]

$$V_r = \left(V_s^{\,p} - V_{bl}^{\,p} \right)^{1/p} \quad , \tag{2}$$

where V_{bl} is the ballistic limit velocity, and p is the empirical constant used to best fit the data with the least squares method. We point out that the data in Figs. 6-8 for β=0°, 15°, and 30° are in very close agreement with the curve-fits except for the hard core data for β=30° near the ballistic limit velocity. However, Fig. 9 for β=45° shows some scatter about the curve-fits. Table 3 presents the coefficients of determination for these curve-fits.

The measured ballistic-limit velocities for the APM2 bullets and steel cores are listed in Table 4 for β=0°, 15°, 30°, and 45°. Figures 6-9 and Table 4 show relatively small differences between results for the APM2 bullets and the hard steel cores. Thus, the brass jacket and lead

8

filler had a relatively small effect on the perforation process even though the masses of the APM2 bullet and hard steel core are 10.7g and 5.25g respectively. We conclude that the hard steel core dominates the perforation process.

Cavity-Expansion Model

We give a full discussion of the cylindrical, cavity-expansion, perforation models in [5,11,12]. Briefly, the aluminum plate deformations are dominated by ductile hole-growth and the holes had nearly the diameter of the projectile shanks. To approximate ductile hole growth, the cylindrical, cavity-expansion method idealizes the target as thin independent layers that are compressed perpendicular to the perforation direction. Thus, the analysis is simplified to one-dimensional motion in the radial plate direction for an elastic-plastic material. We perform a cylindrically symmetric, cavity-expansion analysis, use these results to develop the perforation equations, and obtain closed-form equations that predict the ballistic-limit V_{bl} and residual V_r velocities. The perforation equations are given by

$$V_{bl} = \left(\frac{2\sigma_s}{\rho_p} \frac{h}{(L+k_1 l)} \right)^{1/2} \left[1 + C + \frac{2}{3}C^2 \right]^{1/2} \tag{3}$$

$$V_r = V_{bl} \left[\left(\frac{V_s}{V_{bl}} - 1 \right) \right]^{1/2} \left[1 - C + \frac{1}{2}C^2 \right] \quad , \tag{4}$$

where

$$C = \frac{h}{(L+k_1 l)} \frac{\rho_t}{\rho_p} B_o N(\psi) \tag{5}$$

$$\sigma_s = \frac{Y}{\sqrt{3}} \left\{ 1 + \left[\frac{E}{\sqrt{3}Y} \right]^n \int_0^b \frac{(-\ln x)^n}{1-x} dx \right\} \quad , \, b = 1 - \gamma^2 \tag{6}$$

$$\gamma^2 = \frac{2(1+v)Y}{\sqrt{3}E} \tag{7}$$

9

$$k_1 = \left(4\psi^2 - \frac{4\psi}{3} + \frac{1}{3}\right) - \frac{4\psi^2(2\psi-1)}{(4\psi-1)^{1/2}} \sin^{-1}\left[\frac{(4\psi-1)^{1/2}}{2\psi}\right] \qquad (8)$$

$$N(\psi) = 8\psi^2 \ln\left(\frac{2\psi}{2\psi-1}\right) - (1+4\psi) \quad , \qquad (9)$$

where h is the target plate thickness, σ_s is the quasi-static radial stress required to open a cylindrical cavity, B_o is a curve fitting parameter obtained from the dynamic radial stress as a function of expansion velocity as described in [5], and k_1 and $N(\psi)$ are functions of the ogive-nose shape. Other parameters were defined in previous sections that describe the bullet and target plate.

Unfortunately, there is a misprint in [5,11]. In [5], the term with C in equation (6) should read $[1 - C + C^2/2]$; in [11] the term with C in equations (15) and (21) should also read $[1 - C + C^2/2]$. This misprint is corrected here, and also corrected in the recent paper by Holmen et al. [4]. In addition, our work in [5,11] is for normal impact ($\beta=0^o$) and plates with thickness h. The bullet follows the shot line for oblique impacts, so we use an effective plate thickness in the model for oblique impacts. The effective plate thickness h_e is given by $h_e=h/\cos\beta$, so for this study, $h_e=1.035h$, $1.155h$, and $1.414h$ for $\beta=15^o$, 30°, and 45°, respectively.

For input to the cavity-expansion perforation model, we require the material and geometry properties of the target plate and hard steel core. The target has thickness $h=20$mm and the material properties are listed in Fig. 3. The hard steel core projectile has the geometry described in the Projectiles section of this paper. Other parameters for the model calculated from the target and projectile properties are $B_o=$ 2.8135, $\sigma_s=1.059$GPa , and $N(\psi=3)=0.127$. The value of C depends on the shot line thickness h_e, and $C=$ 0.110, 0.114, 0.127, and 0.156 for $\beta=0^o$, 15°, 30°, and 45°, respectively.

Figures 10-13 show plots of residual velocity versus striking velocity for the data and model predictions. Predictions with $C=0$ neglect the effect of radial target inertia. Figures 10,

11, and 12 for $\beta=0^o$, 15°, and 30° show that the model predictions that include and neglect the inertia C terms in equations (3,4) bound the data. However, predictions in Fig, 13 for $\beta=45^o$ do not bound the data near the ballistic limit velocity. For such a complex problem, we conclude that the cylindrical cavity-expansion model predictions are in good agreement with the data for $\beta=0^o$, 15°, and 30°.

<mark>As previously discussed, the cylindrical, cavity-expansion approximation model for normal impact ($\beta=0^o$) idealizes the target as thin independent layers expanding in the radial direction that is perpendicular to the direction of perforation. Therefore, the analysis is simplified to one-dimensional motion in the radial direction. Thus, the two-dimensional axi-symmetric problem is approximated with a one-dimensional model. For oblique impacts with $\beta=15^o$, 30°, and 45°, we make an additional assumption that the bullet follows the shot line, and we replace the plate thickness h with the shot line distance given by the effective distance $h_e=h/\cos\beta$. Therefore, for the oblique impact problem, we approximate a three-dimensional problem with a one-dimensional model. Thus, the model for oblique impacts becomes less accurate with increasing β.</mark>

Ballistic–Limit Scaling Law for the Bullet

We have shown in previous studies [5,6] and in this work that the hard steel core dominates the perforation process and that the effect of target inertia is small. If we neglect target inertia in equation (3), the predicted ballistic-limit velocity V_{bl} for the hard steel core is given by

$$V_{bl} = \left(\frac{2\sigma_s}{\rho_p} \frac{h}{(L+k_1 l)} \right)^{1/2}. \tag{10}$$

In equation (10), $(L+k_1 l)$ corresponds to the hard steel core geometry, and ρ_p is the hard steel

core density. So for a fixed 7.62mm APM2 bullet, only the terms h and σ_s are variables in equation (10). These observations suggest a scaling law for the bullet of the form

$$V_{bl} = K\left(\sigma_s h\right)^{1/2} \quad , \tag{11}$$

where K is a constant, σ_s is given by equation (6), and h is plate thickness.

Ballistic-limit velocity data for normal impact from our work and Gooch [1,2] are plotted in Fig. 14. The material parameters, plate thickness, and ballistic-limit data are listed in Tables 5 and 6. Figure 14 shows data for plate thicknesses between 20-60mm and five aluminum alloys. The solid line in Fig. 14 is a least squares fit with the value of $K=109\,(\text{m/s})(\text{GPa}\cdot\text{mm})^{-1/2}$. Thus, the ballistic-limit velocities for five aluminum armors impacted by the 7.62mm APM2 bullet are proportional to the square root of the product of the plate thickness and a material strength term.

Summary and Discussion

In this study, we present results from a large number of experiments with 7.62mm APM2 bullets and 20-mm-thick, 6082-T651 aluminum armor plates. We performed experiments with the 10.7g, APM2 bullets and with the 5.25g, hard steel cores contained in the APM2 bullet. A rifle launched these projectiles to striking velocities between 400 and 1000m/s into 20-mm-thick target plates at normal impact ($\beta=0^{\circ}$) and oblique angles of $\beta=15^{\circ}$, 30°, and 45°: Measured residual and ballistic-limit velocities for the full bullet and the hard core were within a few percent for normal impact and all oblique angles. Thus, we showed that the perforation process was dominated by the hard steel core of the bullet. In addition, we conducted large strain, compression tests on the 6082-T651 plate material for input to perforation equations derived from a cavity-expansion model for the steel core projectiles. Model predictions were shown to be in good agreement with measured ballistic-limit and residual velocity measurements. We also

presented a scaling law for the bullet that showed the ballistic-limit velocities were proportional to the square root of the product of plate thickness and a target material strength term.

Acknowledgement

References

1. Gooch WA, Burkins MS, Squillacioti RJ (2007) Ballistic testing of commercial aluminum alloys and alternative processing techniques to increase the availability of aluminum armor. Proceedings of the 23rd International Symposium on Ballistics, Spain: 981-988.

2. Gooch WA (2009) Some 0.30-cal APM2 firing data on 5083-H131. e-mail communication to MJ Forrestal, June 9, 2009.

3. Børvik T, Olovsson L, Dey S, Langseth M (2011) Normal and oblique impact of small arms bullets on AA6082-T4 aluminum protective plates. Int J Impact Eng 38: 577-589.

4. Holmen JK, Johnson J, Jupp S, Hopperstad OS, Børvik T (2013) Effects of heat treatment on the ballistic properties of AA6070 aluminum alloy. Int J Impact Eng 57: 119-133.

5. Børvik T, Forrestal MJ, Warren TL (2010). Perforation of 5083-H116 aluminum armor plates with ogive-nose rods and 7.62mm APM2 bullets. Exp Mech 50: 969-978.

6. Forrestal MJ, Børvik T, Warren TL (2010). Perforation of 7075-T651 aluminum armor plates with 7.62mm APM2 bullets. Exp Mech 50: 1245-1251.

7. Kawahara WA (1990) Effects of specimen design in large-strain compression. Experimental Techniques 14: 58-60.

8. Lovato ML, Stout MG (1992) Compression testing techniques to determine the stress/strain behavior of metals subject to finite deformation. Metallurgical Transactions A 23A: 935-951.

9. Lambert JP, Jonas GH (1976) Towards standardization in terminal ballistic testing: velocity representation. Ballistic Research Laboratories, Report BRL-R-1852, USA.

10. Zukas JA (1990) High velocity impact dynamics, John Wiley and Sons, Inc., New York, pp. 424-427.

11. Forrestal MJ, Warren TL (2009) Perforation equations for conical and ogival nose rigid projectiles into aluminum target plates. Int J Impact Eng 36: 220-225.

12. Forrestal MJ, Romero LA (2007) Comment on "Perforation of aluminum plates with ogive-nose steel rods at normal and oblique impacts". Int J Impact Eng 34: 1962-1964.

13. Forrestal MJ, Luk VK, Brar NS (1990) Perforation of aluminum armor plates with conical-nose projectiles. Mechanics of Materials 10: 97-105.

14. Piekutowski AJ, Forrestal MJ, Poormon KL, Warren TL (1996) Perforation of aluminum plates with ogive-nose steel rods at normal and oblique impacts. Int J Impact Eng 18: 877-887.

15. Forrestal MJ, Luk VK, Rosenberg Z, Brar NS (1992) Penetration of 7075-T651 aluminum targets with ogival-nose projectiles. Int J Solids Struct 29: 1729-1736.
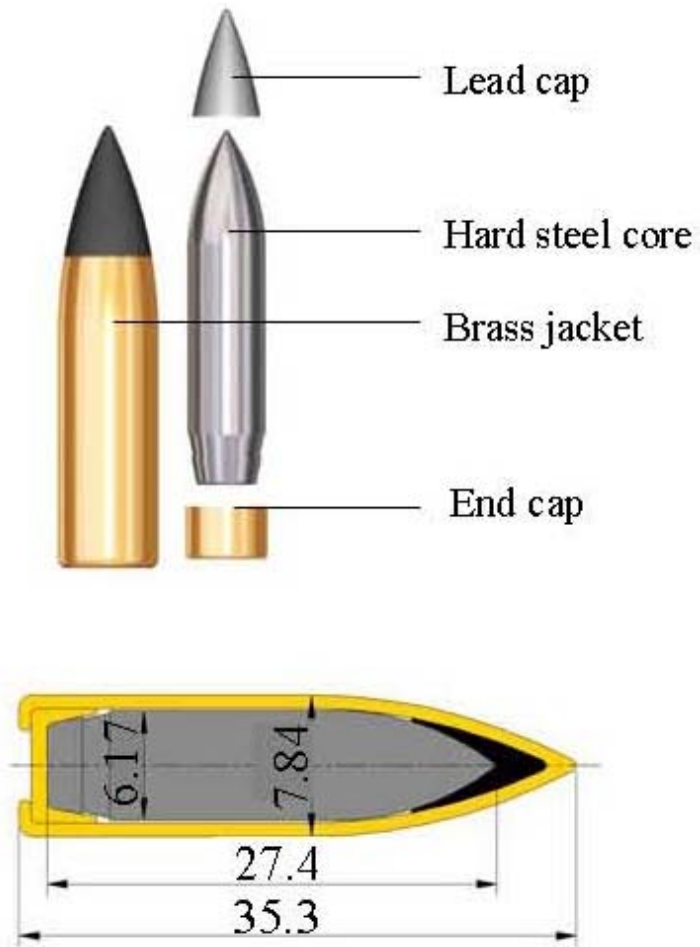
Figure Captions

Fig.1 Geometry of the 7.62mm APM2 bullet (in mm).

Fig.2 Compression test deformation images.

Fig.3 Compression stress-strain data and power-law fit with E=69GPa, v=0.33, Y=265MPa, n=0.060, ρ_t=2,710kg/m^3, and coefficient of determination=0.9980.

Fig.4 High-speed images showing the perforation process of a 20-mm-thick, 6082-T651 aluminum plate impacted by a 7.62mm APM2 bullet (V_s=568m/s, V_r=290m/s).

Fig.5 High-speed images showing the perforation process of a 20-mm-thick, 6082-T651 aluminum plate impacted by the 6.17-mm-diameter, hard steel core (V_s=727m/s, V_r=519m/s).

Fig.6 Residual versus striking velocities for the bullet (V_{bl}=501m/s, p=2.19) and steel core (V_{bl}=514m/s, p=1.97). Normal impact, β=0°.

Fig.7 Residual versus striking velocities for the bullet (V_{bl}=516m/s, p=2.18) and steel core (V_{bl}=535m/s, p=2.14). Oblique impact, β=15°.

Fig.8 Residual versus striking velocities for the bullet (V_{bl}=580m/s, p=2.46) and steel core (V_{bl}=597m/s, p=2.14). Oblique impact, β=30°.

Fig.9 Residual versus striking velocities for the bullet (V_{bl}=718m/s, p=2.74) and steel core (V_{bl}=723m/s, p=2.33). Oblique impact, β=45°.

Fig.10 Comparison of predicted and measured striking versus residual velocity for the hard steel core only of an APM2 bullet impacting 20mm AA6082-T651 target plates. Normal impact β=0°.

Fig.11 Comparison of predicted and measured striking versus residual velocity for the hard steel core only of an APM2 bullet impacting 20mm AA6082-T651 target plates. Oblique impact β=15°.

Fig.12 Comparison of predicted and measured striking versus residual velocity for the hard steel core only of an APM2 bullet impacting 20mm AA6082-T651 target plates. Oblique impact β=30°.

Fig.13 Comparison of predicted and measured striking versus residual velocity for the hard steel core only of an APM2 bullet impacting 20mm AA6082-T651 target plates. Oblique impact β=45°.

Fig.14 Scaling law and data for the 7.62mm APM2 bullet and aluminum armor plates.

Tables

Table 1 Test data for APM2 bullets and 20-mm-thick 6082-T651 aluminum plates.

Table 2 Test data for the hard steel cores and 20-mm-thick 6082-T651 aluminum plates.

Table 3 Coefficients of determination for Lambert-Jonas curve-fit.

Table 4 Ballistic-limit velocity data, V_{bl}(m/s).

Table 5 Material parameters.

Table 6 Ballistic-limit velocities.

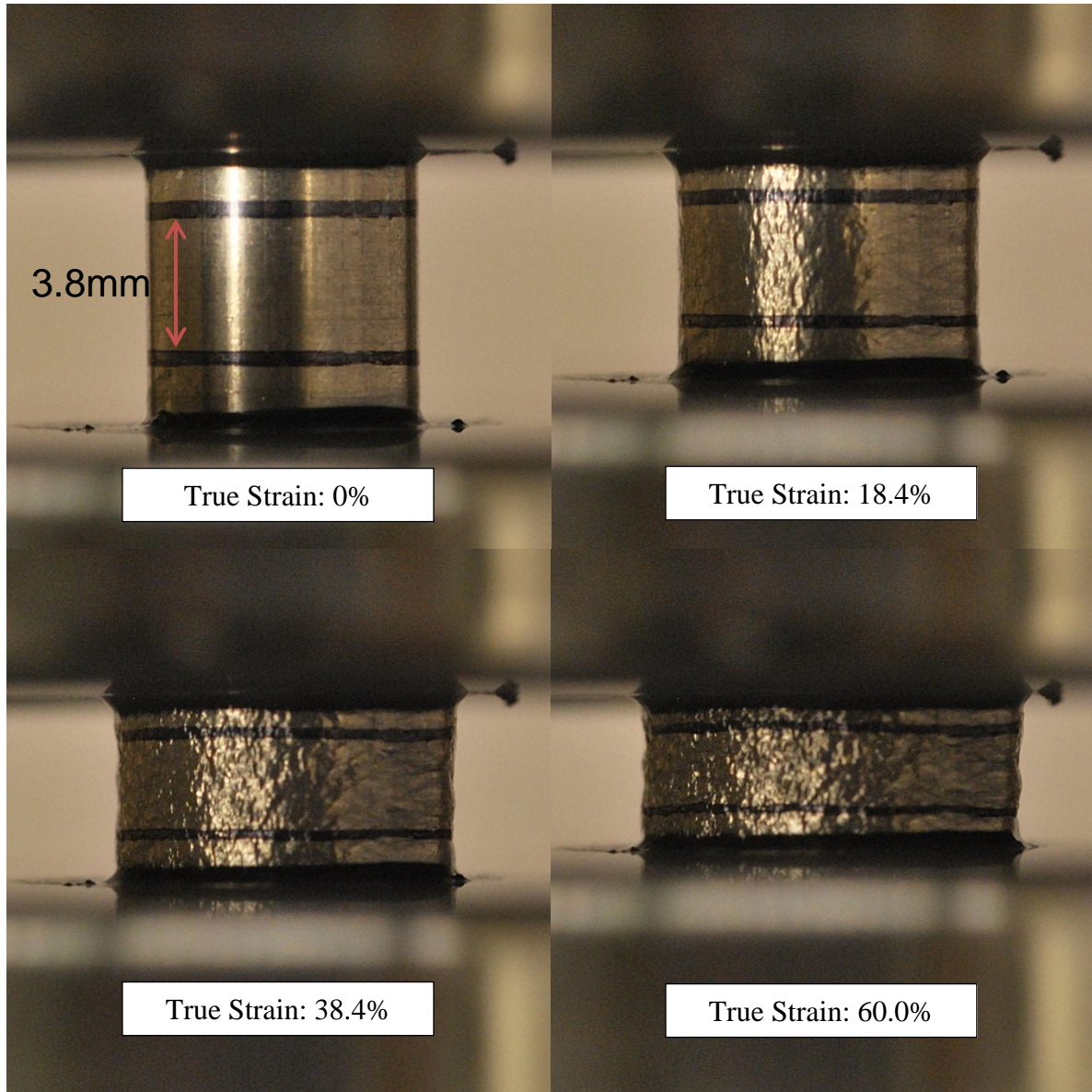**Fig.1** Geometry of the 7.62mm APM2 bullet (in mm).
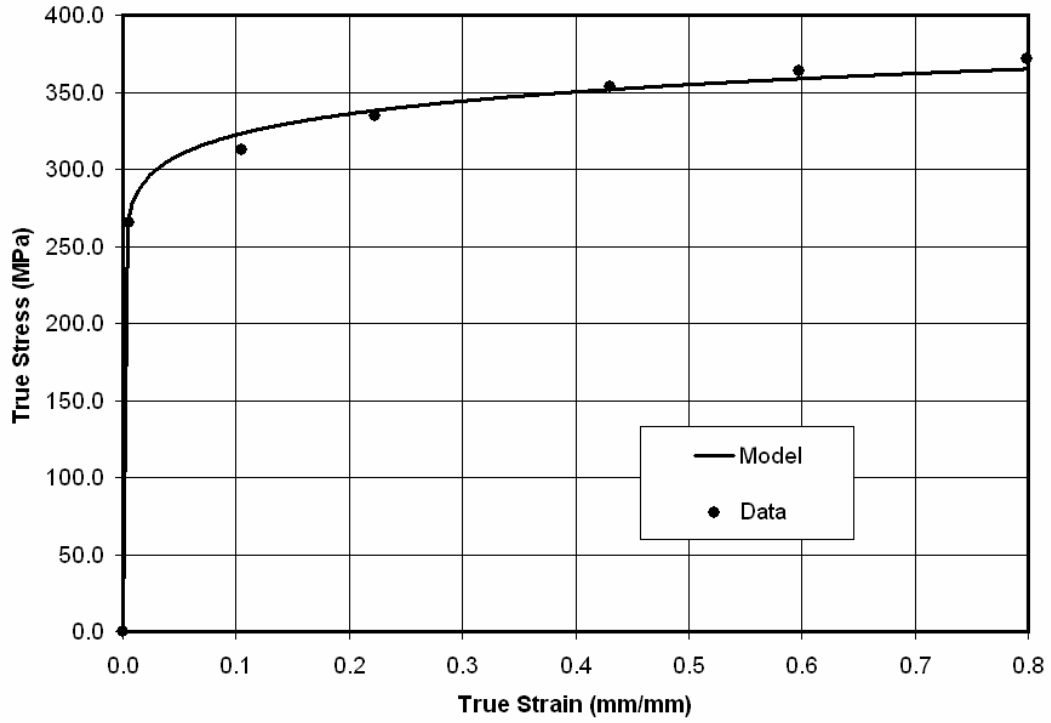
Fig.2 Compression test deformation images.

Fig.3 Compression stress-strain data and power-law fit with E=69GPa, v=0.33, Y=265MPa, n=0.060, ρ_t=2,710kg/m^3, and coefficient of determination=0.9980.
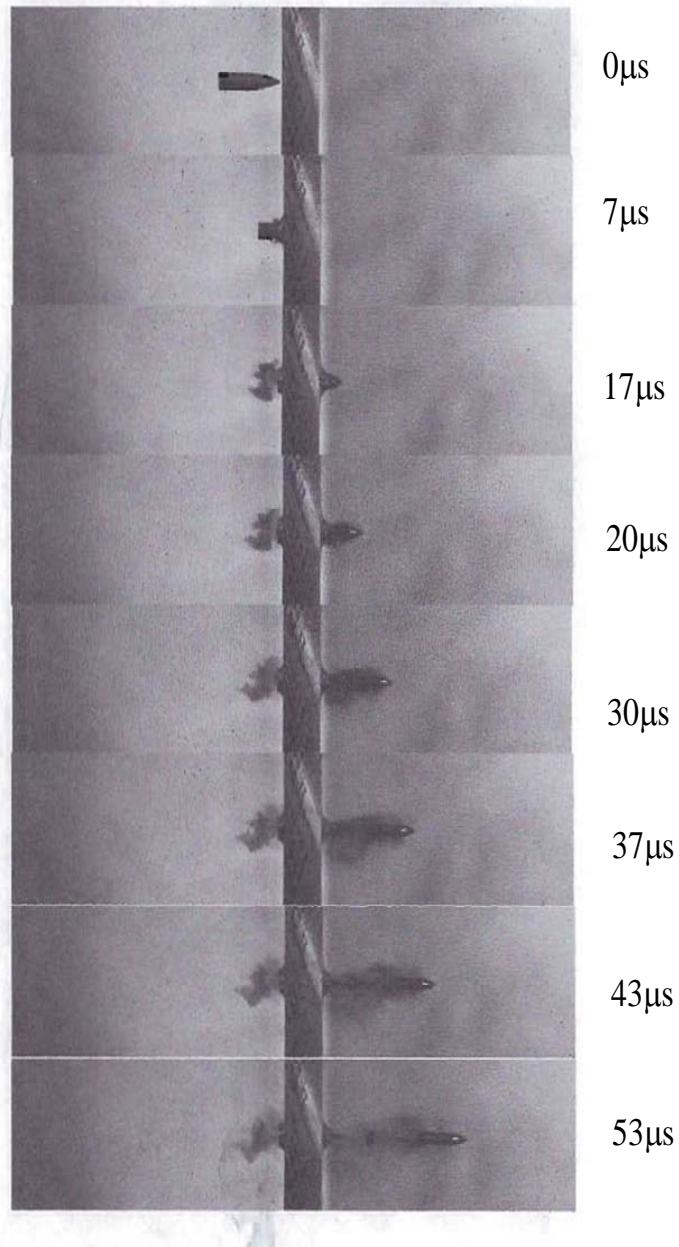
Fig.4 High-speed images showing the perforation process of a 20-mm-thick, 6082-T651 aluminum plate impacted by a 7.62mm APM2 bullet (V_s=568m/s, V_r=290m/s).
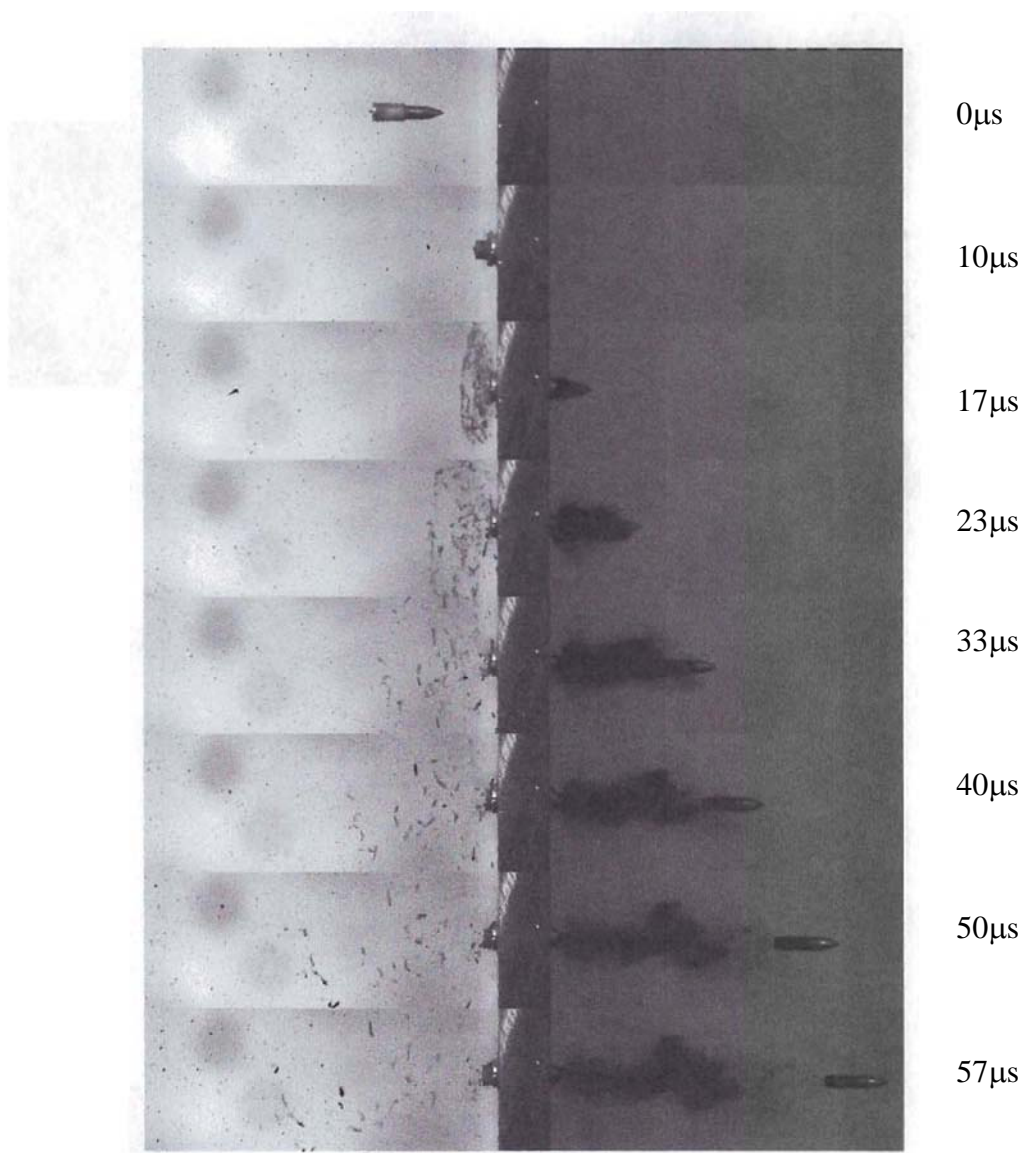
0μs

10μs

17μs

23μs

33μs

40μs

50μs

57μs

Fig.5 High-speed images showing the perforation process of a 20-mm-thick, 6082-T651 aluminum plate impacted by the 6.17-mm-diameter, hard steel core (V_s=727m/s, V_r=519m/s).

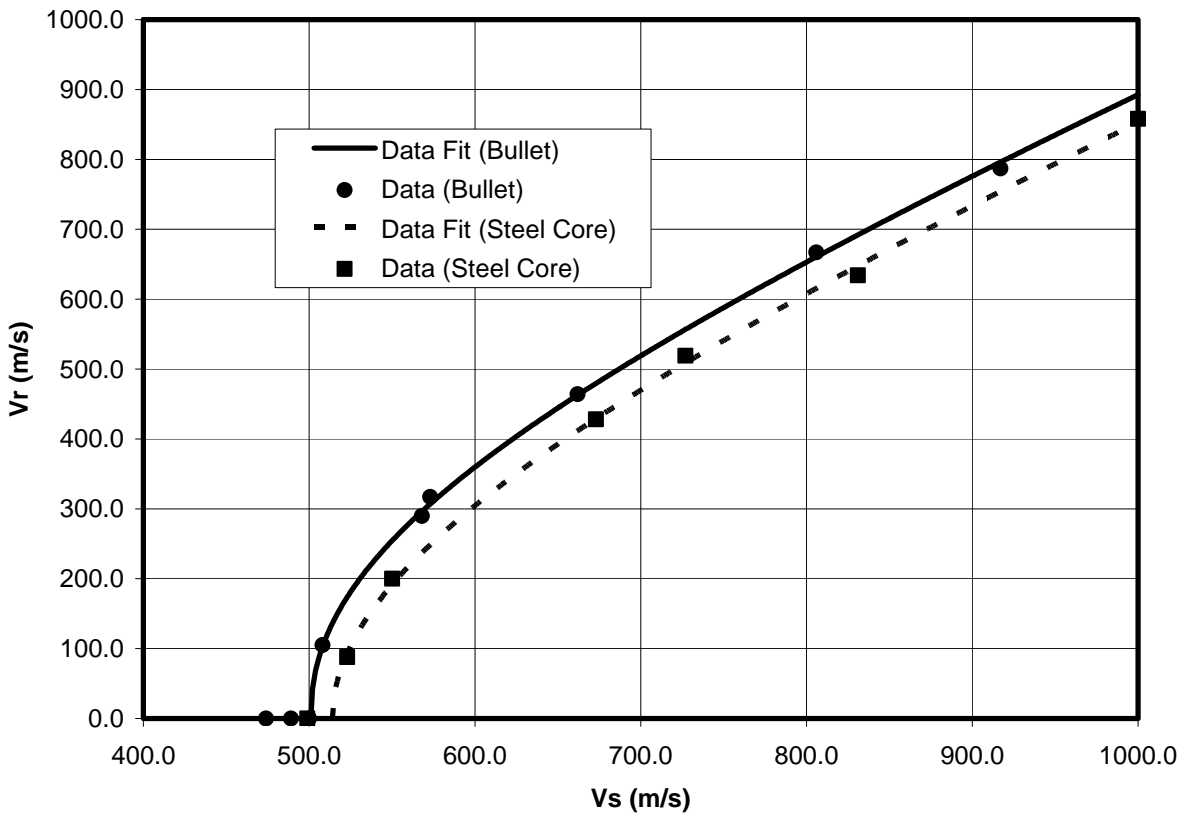**Fig.6** Residual versus striking velocities for the bullet (V_{bl}=501m/s, p=2.19) and steel core (V_{bl}=514m/s, p=1.97). Normal impact, β=0°.

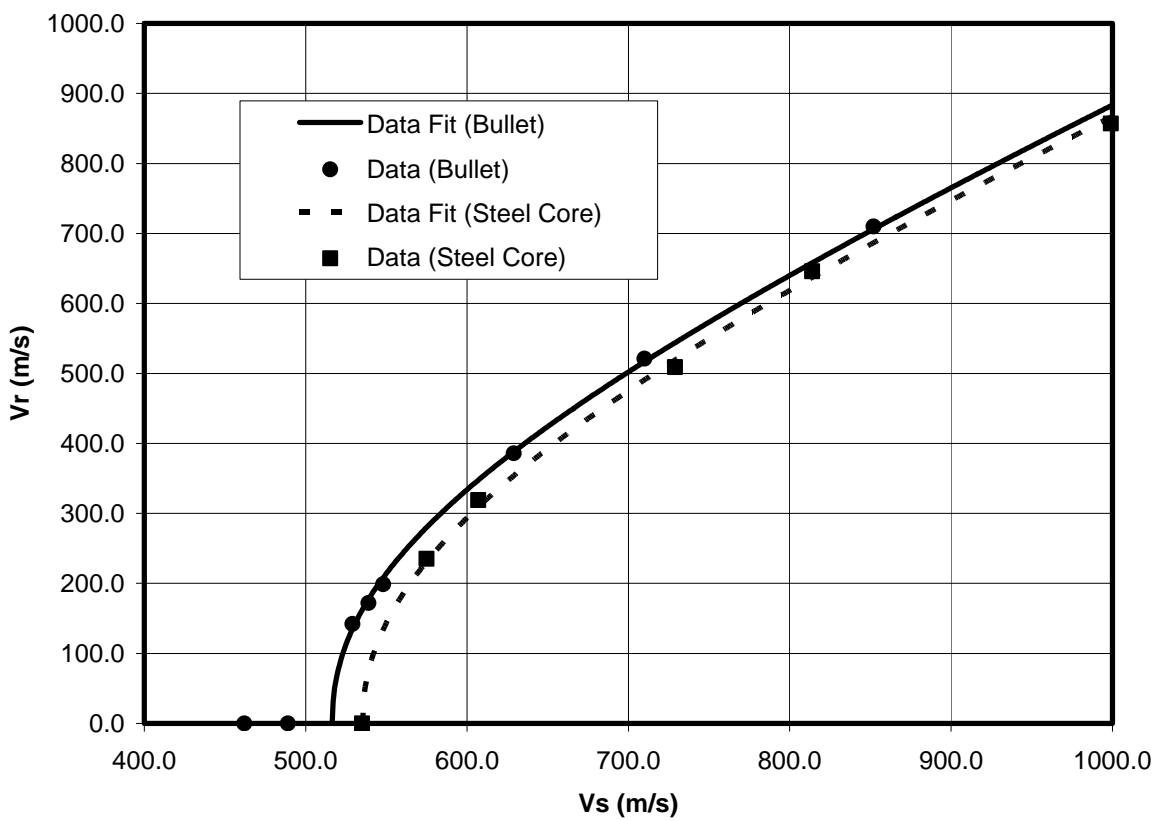**Fig.7** Residual versus striking velocities for the bullet (V_{bl}=516m/s, p=2.18) and steel core (V_{bl}=535m/s, p=2.14). Oblique impact, β=15°.
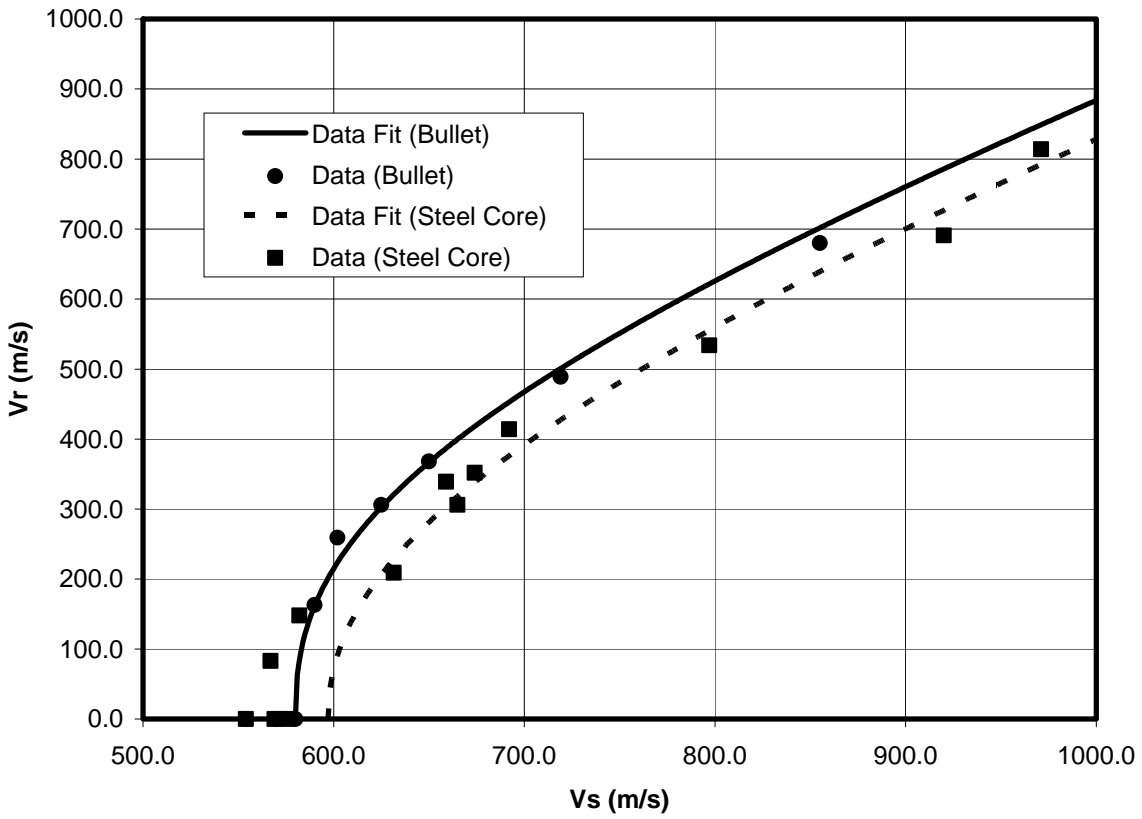
Fig.8 Residual versus striking velocities for the bullet (V_{bl}=580m/s, p=2.46) and steel core (V_{bl}=597m/s, p=2.14). Oblique impact, β=30°.

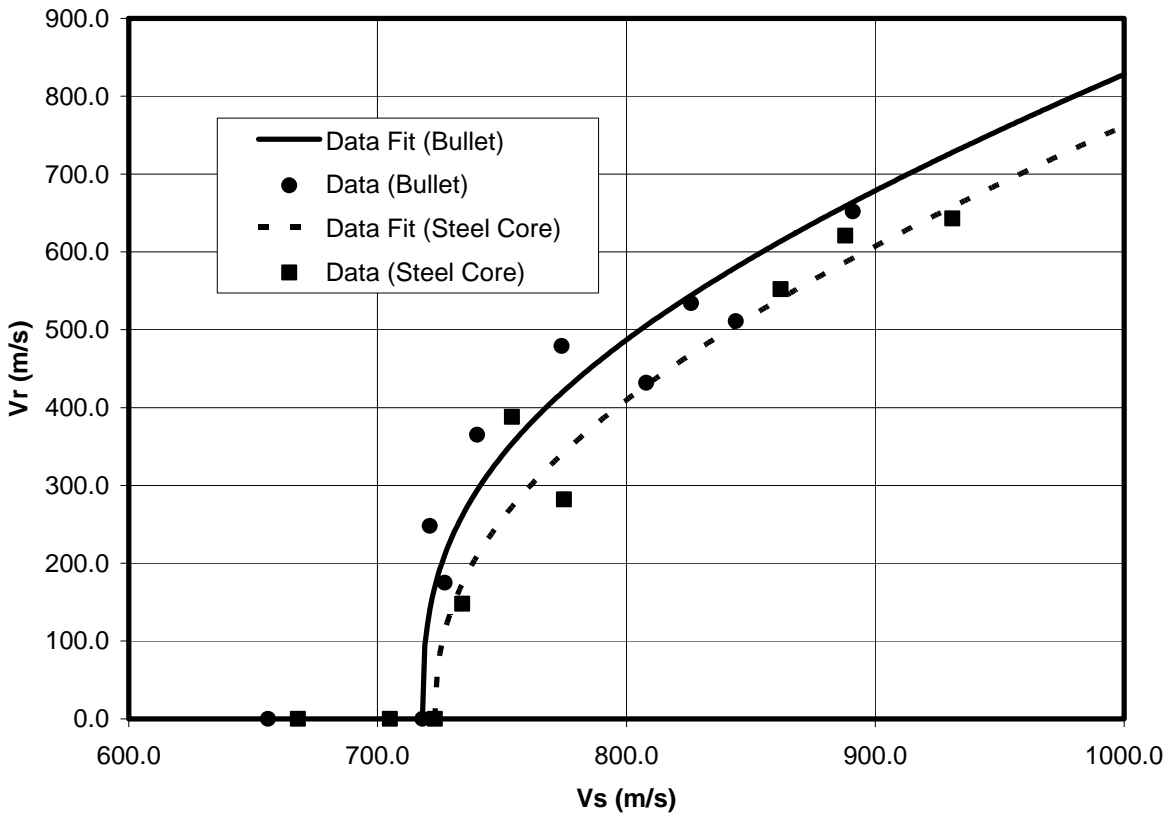**Fig.9** Residual versus striking velocities for the bullet (V_{bl}=718m/s, p=2.74) and steel core (V_{bl}=723m/s, p=2.33). Oblique impact, β=45°.

Fig.10 Comparison of predicted and measured striking versus residual velocity for the hard steel core only of an APM2 bullet impacting 20mm AA6082-T651 target plates. Normal impact $\beta=0^{\circ}$.

Fig.11 Comparison of predicted and measured striking versus residual velocity for the hard steel
core only of an APM2 bullet impacting 20mm AA6082-T651 target plates. Oblique
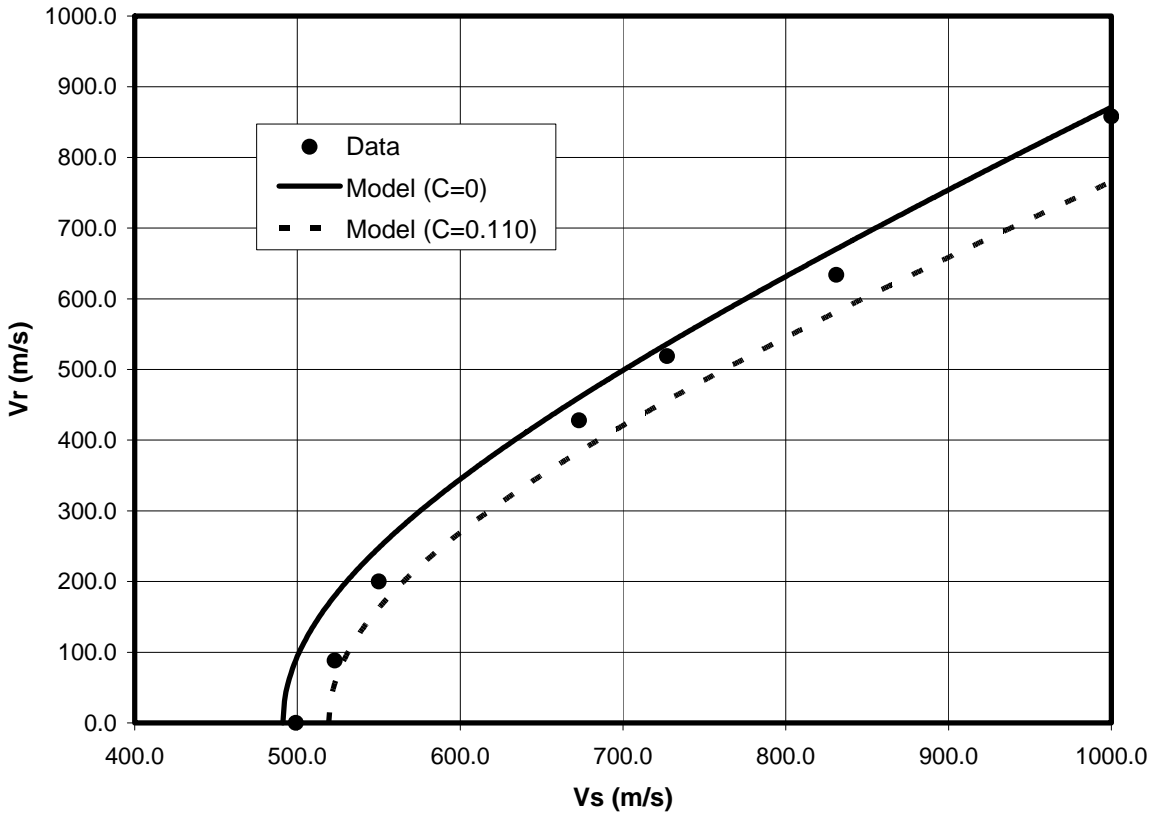impact $\beta=15^{o}$.

Fig.12 Comparison of predicted and measured striking versus residual velocity for the hard steel core only of an APM2 bullet impacting 20mm AA6082-T651 target plates. Oblique impact $\beta=30^\circ$.
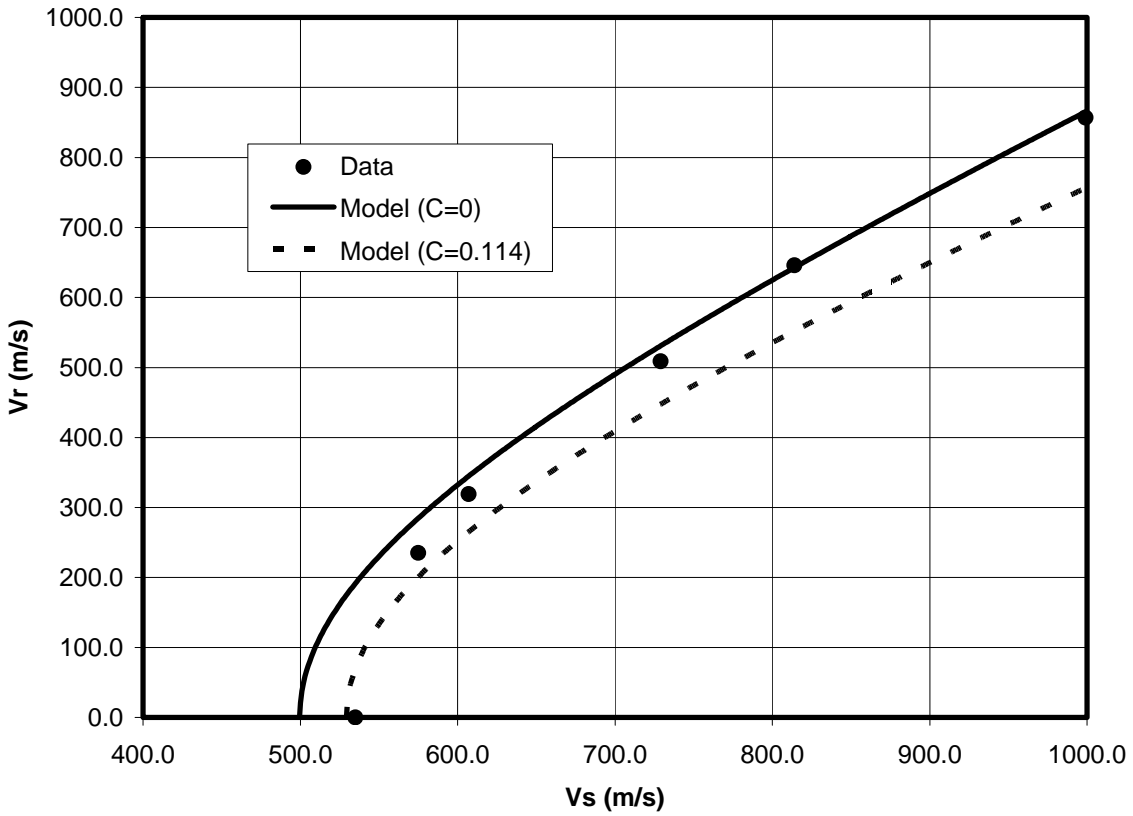
Fig.13 Comparison of predicted and measured striking versus residual velocity for the hard steel core only of an APM2 bullet impacting 20mm AA6082-T651 target plates. Oblique impact $\beta=45^{\circ}$.
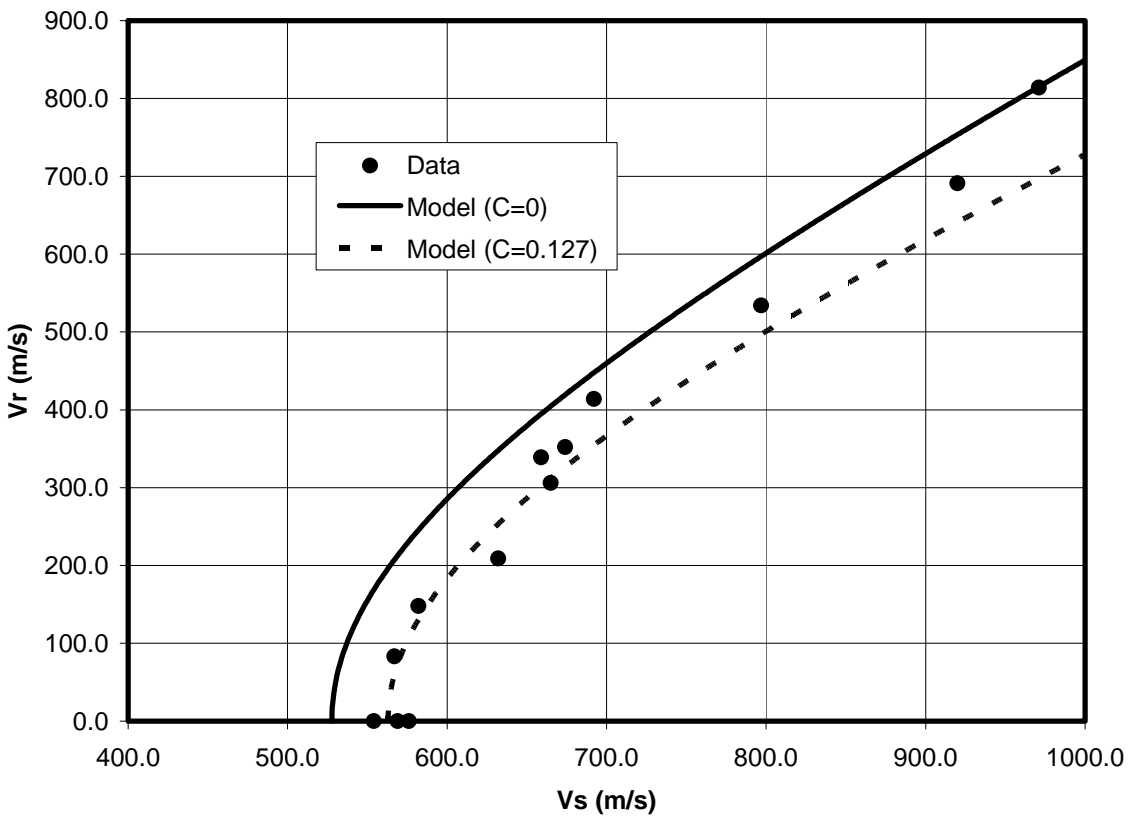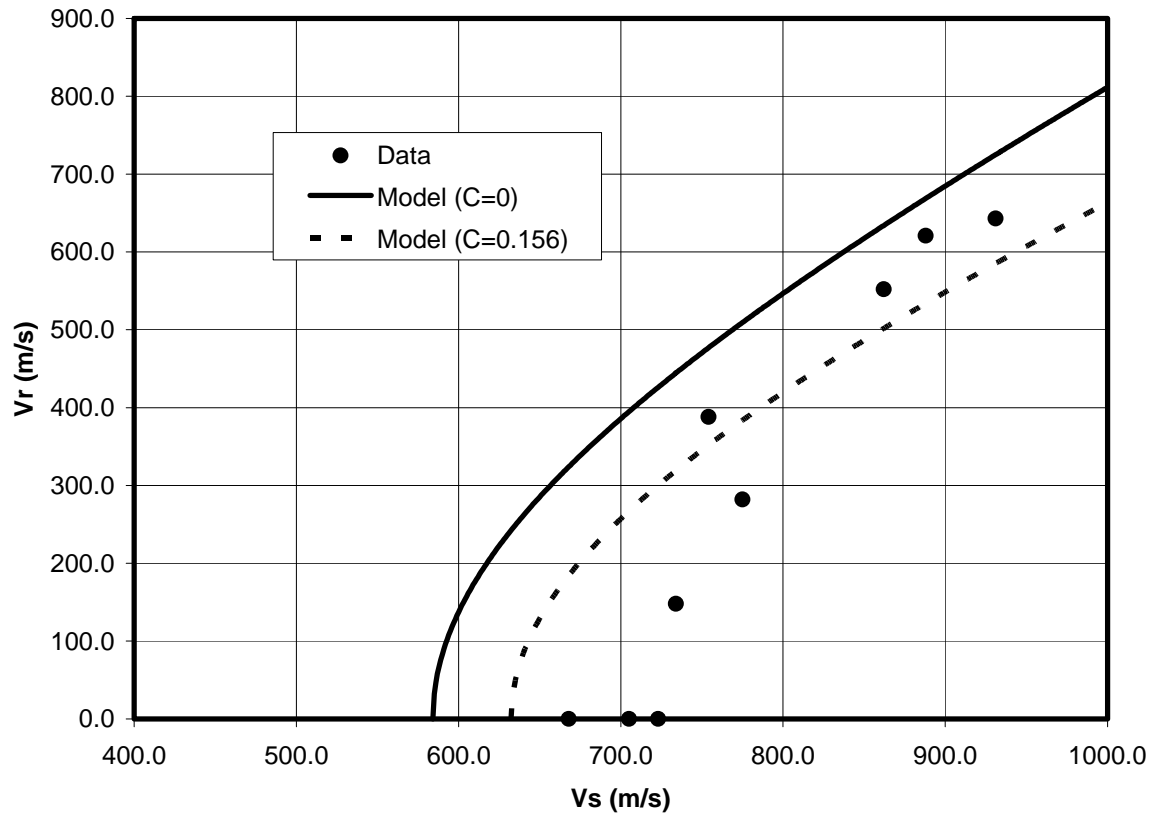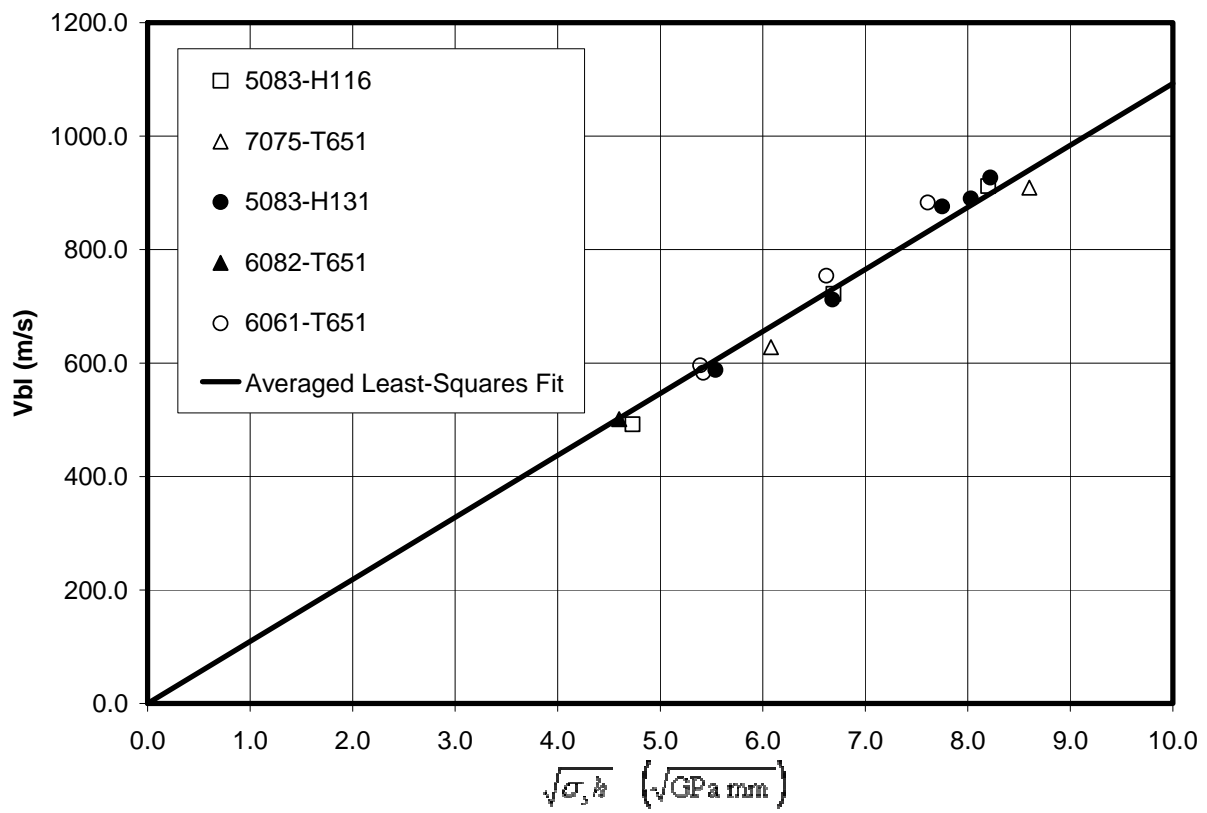
Fig.14 Scaling law and data for the 7.62mm APM2 bullet and aluminum armor plates.

Table 1 Test data for APM2 bullets and 20-mm-thick 6082-T651 aluminum plates.

β (degrees)	V_s (m/s)	V_r (m/s)
0	474	0
0	489	0
0	500	0
0	508	105
0	568	290
0	573	317
0	662	464
0	806	667
0	917	787
15	462	0
15	489	0
15	529	142
15	539	172
15	548	199
15	629	386
15	710	521
15	852	710
30	554	0
30	570	0
30	580	0
30	590	163
30	602	259
30	625	306
30	650	368
30	719	489
30	855	680
45	656	0
45	718	0
45	721	248
45	727	175
45	740	365
45	774	479
45	808	432
45	826	534
45	844	511
45	891	652

Table 2 Test data for the hard steel cores and 20-mm-thick 6082-T651 aluminum plates.

β (degrees)	V_s (m/s)	V_r (m/s)
0	499	0
0	523	88
0	550	200
0	673	428
0	727	519
0	831	634
0	1000	858
15	535	0
15	575	235
15	607	319
15	729	509
15	814	646
15	999	857
30	554	0
30	567	83
30	569	0
30	576	0
30	582	148
30	632	209
30	659	339
30	665	306
30	674	352
30	692	414
30	797	534
30	920	691
30	971	814
45	668	0
45	705	0
45	723	0
45	734	148
45	754	388
45	775	282
45	862	552
45	888	621
45	931	643

Table 3 Coefficients of determination for Lambert-Jonas curve-fit.

Degrees	Bullet	Steel Core
0	0.9994	0.9993
15	0.9994	0.9992
30	0.9901	0.9569
45	0.8998	0.9468

Table 4 Ballistic-limit velocity data, V_{bl}(m/s).

Impact Angle	$\beta=0^{o}$	$\beta=15^{o}$	$\beta=30^{o}$	$\beta=45^{o}$
APM2 Bullet	501	516	580	718
Hard Steel Core	514	535	597	723

Table 5 Material parameters.

Material	E (GPa)	v	Y (MPa)	n	σ_s (GPa)	Reference
5083-H116	71	0.33	240	0.108	1.12	[5]
5083-H131	70	0.33	276	0.084	1.18	[13]
6061-T651	69	0.33	262	0.085	1.13	[14]
6082-T651	69	0.33	265	0.060	1.06	Fig. 3
7075-T651	71	0.33	520	0.060	1.85	[15]

Table 6 Ballistic-limit velocities.

Material	h (mm)	V_{bl} (m/s)	Reference
5083-H116	20.0	492	[5]
5083-H116	40.0	722	[5]
5083-H116	60.0	912	[5]
5083-H131	26.0	588	[2]
5083-H131	37.8	712	[2]
5083-H131	50.9	876	[2]
5083-H131	54.7	890	[2]
5083-H131	57.2	927	[2]
6061-T651	25.7	596	[1]
6061-T651	26.0	583	[1]
6061-T651	38.8	754	[1]
6061-T651	51.2	883	[1]
6082-T651	20.0	501	Table 3
7075-T651	20.0	628	[6]
7075-T651	40.0	909	[6]